

UC Santa Barbara

UC Santa Barbara Electronic Theses and Dissertations

Title

Development of Optical Techniques for Probing Quantum Materials

Permalink

<https://escholarship.org/uc/item/1jj663c4>

Author

Ratcliff, Noah

Publication Date

2022

Peer reviewed|Thesis/dissertation

UNIVERSITY OF CALIFORNIA

Santa Barbara

Development of Optical Techniques for Probing Quantum Materials

A Thesis submitted in partial satisfaction of the
requirements for the degree Master of Science
in Materials

by

Noah Alexander Ratcliff

Committee in charge:

Professor John Harter, Chair

Professor Stephen Wilson

Professor Susanne Stemmer

March 2022

The thesis of Noah Alexander Ratcliff is approved.

Susanne Stemmer

Stephen Wilson

John Harter, Committee Chair

March 2022

Development of Optical Techniques for Probing Quantum Materials

Copyright © 2022

by

Noah Alexander Ratcliff

ACKNOWLEDGEMENTS

This manuscript is dedicated to my parents. Without their love and support I would've never made it this far. I'd like to thank John Harter for giving me the opportunity to contribute to the inception of a state-of-the-art optics lab. I'd also like to thank my dog, Little Dog, for always being by my side. Finally, I'd like to thank my nemesis and best friend Claudia Nelson, for her unwavering support during trying times. Section II of this thesis is adapted from work published in *Physical Review Materials* 3 (2019): 091401. Russell, R., N. Ratcliff, K. Ahadi, L. Dong, S. Stemmer, and J. W. Harter. The thesis author shared the role of the primary author of this paper with Ryan Russell. Section III of this thesis is adapted from work published in *Physical Review Materials* 5 (2021): L111801. Ratcliff, N., L. Hallett, B. R. Ortiz, S. D. Wilson, and J. W. Harter. The thesis author is the primary author of this paper.

ABSTRACT

Development of Optical Techniques for Probing Quantum Materials

by

Noah Alexander Ratcliff

Quantum materials are a growing field of interest in condensed matter physics and materials science due to their manifestation of quantum mechanical effects on the macroscale. Interactions between the charge, spin, lattice, and orbital degrees of freedom, combined with topology and often reduced dimensionality lead to the emergence of electronic ground states which defy understanding in terms of classical physics. Within the field of quantum materials, particular interest is placed on unconventional superconductors as possible candidates for use in quantum information science. Considerable inquiry is focused on the pairing mechanism in unconventional superconductors, as well as interplay between superconducting states and adjacent low-temperature states such as charge density wave (CDW) order and ferroelectricity. This thesis focuses on optical characterization of the quantum materials SrTiO_3 and CsV_3Sb_5 , both unconventional superconductors. I will discuss the methods used to characterize these materials: second harmonic generation (SHG) and pump-probe spectroscopy. The results I have obtained clarified interesting and previously ambiguous phenomena in these materials: SHG techniques supported a connection between ferroelectricity and superconductivity in SrTiO_3 , pump-probe spectroscopy explained the origin of CDW order in CsV_3Sb_5 .

TABLE OF CONTENTS

I. Introduction	1
II. Second Harmonic Generation on SrTiO ₃	3
A. SrTiO ₃	3
B. Methods.....	4
C. Results	5
D. Conclusion	9
II. Pump-Probe Transient Reflectivity on CsV ₃ Sb ₅	10
A. CsV ₃ Sb ₅	10
B. Methods.....	11
C. Results	11
D. Conclusion	17
III. Conclusion	17
References.....	18

LIST OF FIGURES

Figure 1. Temperature dependence of resistivity and SHG response in SrTiO ₃	6
Figure 2. SHG-RA determines the symmetry of the ferroelectric phase.....	7
Figure 3. Ising model of the ferroelectric phase transition in SrTiO ₃	9
Figure 4. Coherent phonon spectroscopy data for CsV ₃ Sb ₅	12
Figure 5. Behavior near the CDW phase transition.....	13
Figure 6. First-principles phonon calculations.	15

I. Introduction

Quantum materials is a subset of condensed matter physics research driven by the investigation of emergent properties of materials. There is a growing interest in the exotic properties quantum materials possess, including non-trivial topology, quantum fluctuations, quantum coherence and high-temperature superconductivity. Current research in the field is focused on discovery and characterization of materials whose electronic properties cannot be understood semi-classically. In fact, the field of quantum materials was formerly known as the field of strongly correlated electronic systems; in this regime, a non-negligible Coulomb interaction invalidates the simple picture of a non-interacting Fermi gas of electrons. Quantum materials research unifies researchers working across the disparate academic disciplines of materials science, physics, and engineering.

Characterizing novel phases of matter is essential to condensed matter and materials science research. Optical techniques such as SHG and pump-probe spectroscopy are ideal tools for uncovering valuable information about quantum materials. SHG is acutely sensitive to inversion symmetry breaking, while pump-probe spectroscopy can reveal the frequency and lifetime of zone centered modes. Both of these techniques probe the optical properties of the materials of interest, which are, at their most basic level, determined by the frequency dependent optical conductivity, dielectric function, and refractive index.

SHG is a nonlinear optical phenomenon that can be exploited to obtain information about symmetry breaking in quantum materials. The leading order electric dipole contribution to SHG response is only allowed wherever inversion symmetry is broken [1].

Mathematically, the nonlinear susceptibility tensor relates the polarization response of the material to the incident electric field via the equation

$$P_i(2\omega) = \chi_{ijk} E_j(\omega) E_k(\omega)$$

where $P_i(2\omega)$ is the electric polarization vector for the second harmonic, and χ_{ijk} is the nonlinear susceptibility tensor, a polar third rank tensor [2]. SHG rotational anisotropy (SHG-RA) is a technique used to determine the SHG susceptibility tensor. This involves the rotation of the scattering plane and measurement of the generated SHG intensity. SHG-RA combined with temperature dependent SHG intensity measurements can be used to detect electronic and structural phase transitions in materials. It can also identify the exact point group of a material at any temperature within experimental limits. SHG measurements can be combined with pump-probe techniques to determine the IR-active modes in a material. In summary, the observation of SHG in a material indicates the breaking of inversion symmetry, and SHG-RA patterns correspond uniquely to each non-centrosymmetric point group.

Examination of the time-dependent response of a material yields valuable insight into the dynamical properties of quantum materials. Pump-probe spectroscopy, the time-domain analog to Raman spectroscopy, is a technique used to measure the transient reflectivity of a material. The technique relies on a high intensity pump beam to excite the sample and a lower intensity probe beam to measure the time-delayed response. Femtosecond time resolution of this data is achieved with the help of femtosecond laser pulses. The typical quantity of interest for this type of experiment is the differential reflectivity $\Delta R/R$, where R is the reflectivity. Measuring the optical response as a function of time delay between the

pump and probe, the response of the sample can be characterized as it returns to equilibrium. The resulting data yields the frequency and lifetime of zone-centered modes. Tracking the temperature dependence of these modes gives information about phase transitions in a material, and one can identify which modes couple to the phase of interest, the pump excitation, and a phonon at a given frequency using Landau theory. Information can also be extracted from the sign of the differential reflectivity, which is known to depend on several electronic parameters such as band filling and band gap renormalization [3]. All in all, information gained from each of these techniques yield different pieces of the puzzle that is quantum materials.

II. Second Harmonic Generation on SrTiO₃

A. SrTiO₃

SrTiO₃ is an oxide superconductor and an incipient ferroelectric in proximity to a polar instability. This ferroelectric ground state is suppressed at low temperatures by quantum fluctuations. Superconductivity is still present within this quantum paraelectric phase despite extremely dilute carrier densities (n_{3D}). This suggests that an unconventional pairing mechanism is responsible for superconductivity in SrTiO₃ as the conventional Bardeen-Cooper-Schrieffer (BCS) theory is inapplicable in the regime where the Fermi energy is less than the Debye frequency.

Ferroelectric fluctuations are suspected to play a role in superconductivity by contributing to electron pairing. However, ferroelectricity and superconductivity are often competing phases; the free carriers needed for superconductivity can screen dipole fields

and prevent long range ordering needed for ferroelectricity. This conflict calls into question the relationship between ferroelectricity and superconductivity in SrTiO₃.

The supposed link between superconductivity and ferroelectricity has motivated studies of the superconducting properties of SrTiO₃ crystals tuned toward ferroelectricity. Epitaxial strain in thin films of SrTiO₃ is known to stabilize ferroelectricity [4] and can enhance the superconducting critical temperature by a factor of two [5]. To clarify the interplay between superconductivity and ferroelectricity in this material, we directly measure the ferroelectric order parameter in compressively strained films of electron-doped SrTiO₃. Standard electrical methods for measuring polarization are prohibited by the metallic nature of the samples; SHG is an all-optical technique that bypasses this obstacle, making it ideal to study polar order in SrTiO₃ [1].

B. Methods

Samarium-doped SrTiO₃ films of thickness 200 nm were grown epitaxially on (001) LSAT substrates via hybrid molecular beam epitaxy. The mechanism for electron doping in these films is the substitution of Sm³⁺ for Sr²⁺. The static in-plane compressive strain was produced by a 1% lattice mismatch between SrTiO₃ and the substrate.

Optical SHG experiments were performed using an ultrafast laser which generated 800 nm, 40 fs pulses at a 10 kHz repetition rate. The laser spot size was 30 μm and the fluence was below 20 $\frac{mJ}{cm^2}$. Data was collected over a wide temperature range from 10 K to 200 K in 5 K steps. The angle of the scattering plane φ was rotated through 360° to collect rotational anisotropy patterns at every temperature point. The polarization dependence of SHG was

determined using both in-plane ($S_{in/out}$) and out-of-plane ($P_{in/out}$) polarization geometries for the incident and outgoing beams.

C. Results

The temperature dependence of SHG intensity and electrical resistivity for three films with varying carrier densities is shown in Figure 1. While a small SHG signal is detected at high temperatures for all films, a sharp onset is observed at low temperatures for the $n_{3D} = 0.6 \times 10^{20} \text{ cm}^{-3}$ and $1.4 \times 10^{20} \text{ cm}^{-3}$ films. We find that the local minima in the resistivity occur at precisely the same temperature as the onset of SHG. We determine that the nonzero SHG response at high temperature exists due to inversion symmetry breaking between the substrate and vacuum. As the temperature is reduced in the two lower-doped films, the ferroelectric phase transition occurs which results in a sudden increase in the SHG response. In the highest doped film, charge carriers screen the dipolar interactions necessary for spontaneous ferroelectricity; this explains the absence of long-range order. These observations demonstrate an unambiguous link between ferroelectricity and electrical transport signatures that have previously been associated with an enhancement of superconductivity [5]. Our results not only settle the question of the origin of the resistivity

anomalies, but in doing so confirm a direct connection between ferroelectricity and superconductivity.

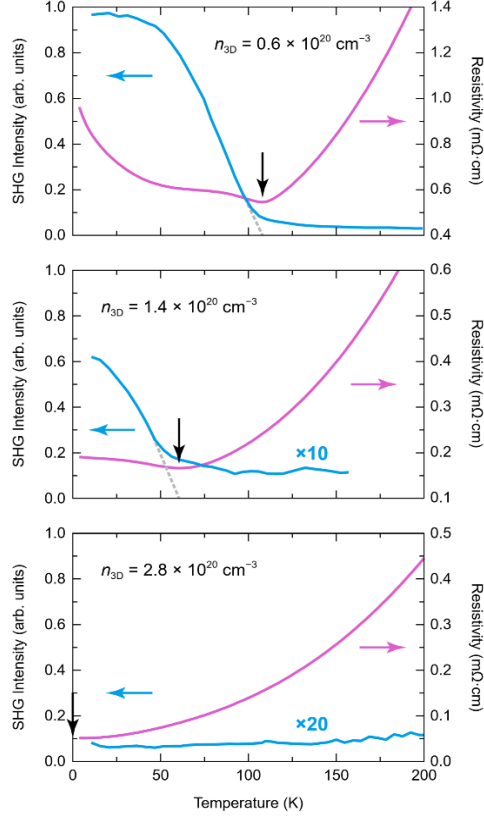


Figure 1: Temperature dependence of resistivity and SHG response in SrTiO₃ films with 3 different carrier densities. Black arrows mark local minima in the resistivity which correlate with the onset temperatures of the ferroelectric order parameter.

In addition to temperature dependent measurements, we performed SHG-RA at low temperatures to determine the symmetry of the ferroelectric order parameter. With this technique we can measure the individual elements of the nonlinear optical susceptibility tensor χ_{ijk} . Figure 2 shows rotational anisotropy patterns in the ferroelectric phase for each polarization channel: S_{in} - S_{out} , S_{in} - P_{out} , P_{in} - S_{out} , and P_{in} - P_{out} . We detect no measurable SHG in the two S_{out} channels, while the response in the P_{out} channels are independent of

the scattering plane angle ϕ . These observations are fully consistent with a $4mm$ (C_{4v}) polar point group, where symmetry considerations yield a predicted response of $I_{SS} = 0$, $I_{SP} \propto |\chi_{zxx}|^2 \sin^2\theta$, $I_{PS} = 0$, and $I_{PP} \propto |\chi_{zzz} \sin^2\theta - |\chi_{zxx} \cos^2\theta|^2 \sin^2\theta$ [6]. In this case, $\theta \approx 30^\circ$ is the angle of incidence for our experimental setup. The measured point group of the strained film in the ferroelectric phase ($4mm$) is a subgroup of the $4/mmm$ tetragonal symmetry of the film at higher temperature; the symmetry lowering is generated by an A_{2u} ferroelectric order parameter directed normal to the plane of the film. The large magnitude of the P_{in} - P_{out} SHG response relative to the S_{in} - P_{out} response indicates that the dominant nonlinear susceptibility element is χ_{zzz} ; this represents out-of-plane anharmonic motion of electrons driven by an out-of-plane electric field.

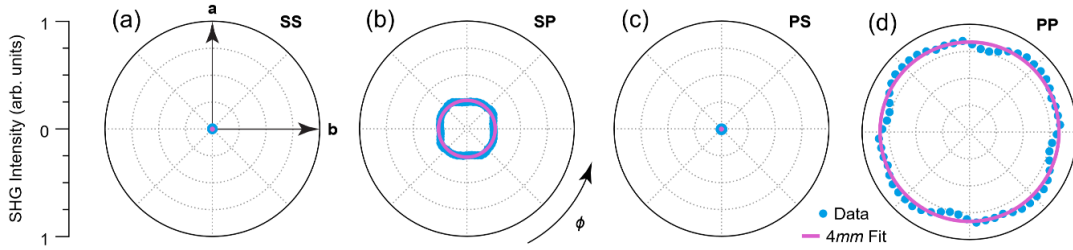


Figure 2: SHG-RA determines the symmetry of the ferroelectric phase; patterns shown for (a) S_{in} - S_{out} , (b) S_{in} - P_{out} , (c) P_{in} - S_{out} , and (d) P_{in} - P_{out} polarization geometries measured at 10K on a $n_{3D} = 0.6 \times 10^{20} \text{ cm}^{-3}$ film.

We used a long-range mean-field Ising model of ferroelectricity to fit the temperature dependence of the SHG intensity, which is shown in Figure 3. In this model, the two opposite polar unit cell distortions stabilized by in-plane compressive strain are equivalent to a bistable Ising order parameter (inset of Figure 3). In addition to a long-range electric dipole-dipole interaction term, a small symmetry-breaking field is included to account for

the dissimilar substrate and vacuum environments on either side of the film. The

Hamiltonian of this model is:

$$H = -\frac{1}{2} \sum_{i,j} U(\mathbf{r}_i - \mathbf{r}_j) p_i p_j - E \sum_i p_i$$

where i and j label unit cells, $p_i = \pm 1$ is the Ising order parameter, $U(\mathbf{r})$ is the dipolar interaction potential energy, and E is the preexisting polarizing field. A mean-field approximation is expected to be accurate because of the long-range nature of the interaction term. Within mean-field theory, the space-averaged order parameter $\langle p \rangle$ satisfies the self-consistency equation

$$\langle p \rangle = \tanh \left(\frac{\bar{U} \langle p \rangle + E}{k_B T} \right)$$

where $\bar{U} = \sum_j \frac{U(\mathbf{r}_j)}{2} = k_B T_C$ determines the critical temperature of the phase transition. \bar{U} is sensitive to the sample carrier density because of electrostatic screening effects. To relate this model to our optical measurements, we assume χ_{ijk} is proportional to the ferroelectric order parameter [7] and include a small temperature-independent background term to account for secondary SHG from the film interfaces. Solutions to the self-consistency equation fitted to the data are plotted in Figure 3. From the field-free fits, we extract bulk critical temperatures of $T_C = 92.4 \pm 0.2 \text{ K}$ for $n_{3D} = 0.6 \times 10^{20} \text{ cm}^{-3}$ and $T_C = 39.1 \pm 1.6 \text{ K}$ for $n_{3D} = 1.4 \times 10^{20} \text{ cm}^{-3}$. Polarizing field energies are on the order of $E/k_B \sim 2 \text{ K}$. While this model is simple, the accuracy with which it fits the data shows that it can capture the essential physics of ferroelectricity in strained SrTiO₃. We emphasize that this is a model of an order-disorder phase transition and not a displacive phase transition,

challenging the hypothesis that superconducting pairing in SrTiO₃ is mediated by polar soft mode fluctuations.

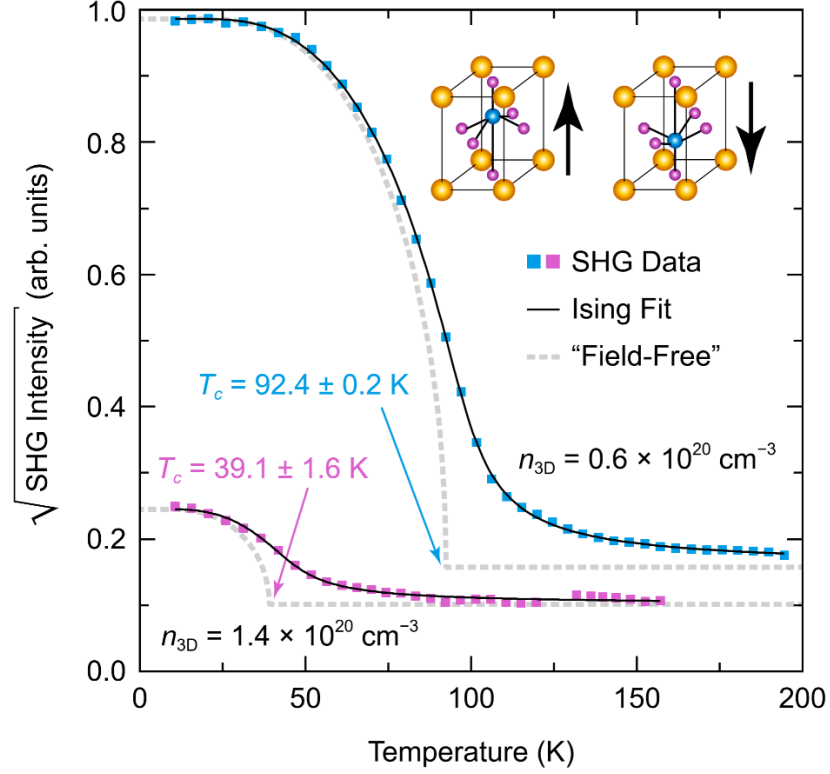


Figure 3: Ising model of the ferroelectric phase transition in SrTiO₃ for samples with two different carrier densities. The square root of SHG intensity, proportional to the ferroelectric order parameter, is reproduced by a long-range mean field Ising model that includes a small symmetry-breaking field. The inset illustrates polar unit cell distortions equivalent to a bistable Ising order parameter. Dashed curves show the hypothetical order parameter in the absence of a field, from which the critical temperature of the phase transition can be estimated.

D. Conclusion

In conclusion, we used temperature dependent SHG as well as SHG-RA to measure the doping and temperature dependence of the out-of-plane ferroelectric polarization in compressively strained SrTiO₃ thin films. We found that enhanced superconductivity

correlated directly with the onset of ferroelectricity. Our results supported a long-suspected connection between ferroelectricity and superconductivity in SrTiO₃ and should prove useful in the development of theoretical models linking the two phases. In particular, the success of the Ising model strengthens the argument for an order-disorder mechanism behind the ferroelectric phase transition, without soft mode fluctuations expected from a displacive transition. Furthermore, the observation of enhanced superconductivity deep within the ferroelectric phase where fluctuations are suppressed undermines their role in superconducting pairing.

III. Pump-Probe Transient Reflectivity on CsV₃Sb₅

A. CsV₃Sb₅

Kagome materials are promising for realizing exotic correlated and topological ground states. Recently, the family of Kagome metals which crystallize in the AV₃Sb₅ structure (A=K, Rb, Cs) has attracted attention for its strong electronic correlations, quasi-two-dimensional nature, superconductivity, and topologically non-trivial band structure. There have already been many complex and interesting properties observed in these Kagome metals, such as the observation of giant anomalous Hall effect [8] and chiral charge order [9] which imply the existence of a time-reversal symmetry breaking instability, despite no evidence of local moment magnetism [10]. Additionally, signatures of nodal quasiparticles [11], multiple superconducting domes [12], [13], and zero-bias conductance peaks inside superconducting vortex cores [14] suggest the possibility of topological superconductivity.

There exists a CDW phase transition at $T_{CDW} = 94K$ for A=Cs [15] which has been identified through anomalies in heat capacity, electrical resistivity, and magnetic

susceptibility. This CDW transition is thought to be driven by a Peierls-like instability at wave vectors connecting the M points at the Brillouin zone boundary. Prior to our work, the exact nature of the CDW order parameter was not well understood; understanding CDW order in these materials will provide insight into the superconducting phase because of its competition with and emergence from the CDW phase [3].

B. Methods

We carried out time-resolved optical reflectivity measurements on a freshly cleaved single crystal of CsV₃Sb₅ mounted in an optical cryostat. The samples were grown using a flux growth method detailed in [10]. A $\sim 100 \frac{\mu\text{J}}{\text{cm}^2}$, 1515nm pump pulse was used to coherently excite the sample and a $\sim 100 \frac{\mu\text{J}}{\text{cm}^2}$, 800nm probe pulse was used to investigate the time dependent optical response. Both pulses were linearly polarized in-plane. Both pulses had a repetition rate of 500 kHz and were generated by a non-collinear optical parametric amplifier. A lock-in amplifier and optical chopper were used to measure the pump-induced change in reflectivity.

C. Results

Figure 4(a) shows the temperature dependence of differential reflectivity $\Delta R(t)/R$ for temperatures between 10 K and 100 K, where t is the time delay between the pump and probe pulses. Below T_{CDW} there is a sharp decrease in the reflectivity immediately after pump excitation, after which it recovers toward a plateau less than the value at negative time delays. Near the phase transition, the transient response at time zero is suppressed and eventually switches sign between 87 K and 97 K. The stark difference in the transient optical response across the CDW phase transition is likely the result of changes in the

density of states and the opening of a gap at the Fermi level[16]. A non-zero signal at negative time delays emerges at the phase transition, indicating ultra-long timescale recovery of ≈ 2 ps. The coherent excitation of multiple Raman-active phonon modes is visible in the recovery, along with a double exponential background.

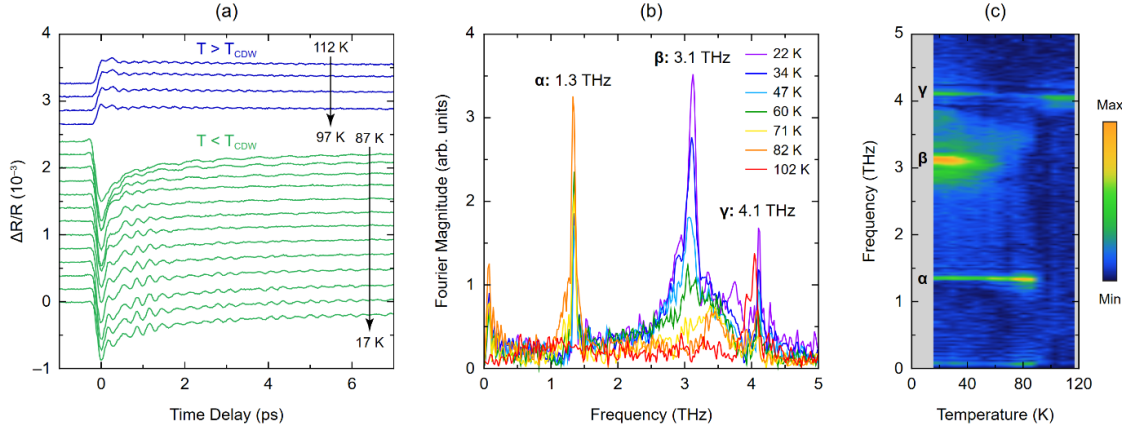


Figure 4: Coherent phonon spectroscopy data for CsV₃Sb₅. (a) Transient reflectivity curves for temperatures above and below the CDW phase transition. Temperatures are roughly evenly spaced and scans are vertically offset. Above T_{CDW} , the reflectivity increases after the pump pulse and a single oscillation frequency is apparent. Below T_{CDW} , the reflectivity decreases after the pump pulse and multiple oscillation frequencies are present. (b) Magnitude of the Fourier transform of the reflectivity oscillations after subtraction of a double exponential background. The three most prominent resonances are labeled α (1.3 THz), β (3.1 THz), and γ (4.1 THz). (c) Two-dimensional temperature-frequency map of the Fourier magnitude of the coherent phonon oscillations. A weak softening of all three modes is seen with increasing temperature.

To elucidate the nature of the coherent phonon oscillations, a double exponential background ($A_0 + A_1 e^{-t/\tau_1} + A_2 e^{-t/\tau_2}$) is fit to the transient reflectivity curves and then subtracted from the data after $t = 100$ fs. The remaining oscillations are Fourier transformed and displayed in Figure 4(b). This data shows that there are three resonance modes present in the material: α at 1.3 THz, β at 3.1 THz, and γ at 4.1 THz. No other clear modes are

detected from 5 to 10 THz. The temperature dependence of the coherent phonon oscillations is displayed in Figure 4(c), which shows a two-dimensional temperature-frequency map of the oscillation spectrum. The γ mode persists above T_{CDW} , β shows up as a broad continuum and does not emerge until 50K, and the α mode shows an abrupt intense appearance at $T \approx 92$ K. This temperature is close to $T_{\text{CDW}} = 94$ K, as determined through heat capacity measurements [15], the small disparity can be explained by sample heating due to the incident beam. All three resonances show a weak frequency softening with increasing temperature, but none show complete softening ($\omega \rightarrow 0$).

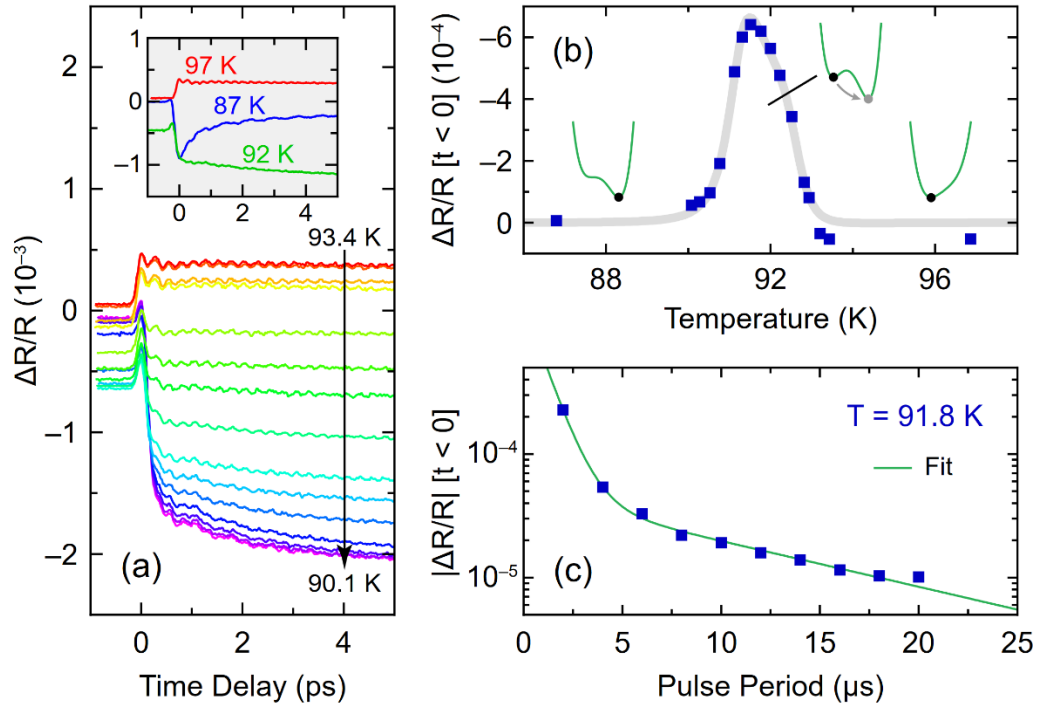


Figure 5: Behavior near the CDW phase transition. (a) Transient reflectivity curves taken at a finely and approximately evenly spaced series of temperatures across the CDW phase transition. Curves are *not* offset and finite $\Delta R/R$ values for $t < 0$ are real. Inset shows pronounced changes in the transient optical response above (red), at (green), and below (blue) T_{CDW} . (b) Average $\Delta R/R$ value for time delays between -1 ps and -0.2 ps versus temperature. A metastable-like divergence in the lifetime of the transient optical response is observed at

T_{CDW} . Insets are sketches of the free energy and the gray curve is a guide to the eye. (c) Average $|\Delta R/R|$ value for negative time delays versus pump-probe pulse period at T_{CDW} , the fit is described in the text.

We also investigated the critical behavior of the CDW phase transition. Figure 5(a) shows transient reflectivity collected within a narrow temperature range centered at T_{CDW} . We observed a pronounced change in the shape of the transient reflectivity curve within 1K of T_{CDW} . Interestingly, we observed an anomalously long recovery behavior demonstrated by the finite $\Delta R/R$ for negative time delays as shown in Figure 5(b). We attribute this to a pump-induced metastable change in the material, where the recovery to equilibrium after one pulse is still occurring when the next pulse arrives. To confirm this, we measured the anomalous $\Delta R(t)/R$ at negative time delays as a function of the pulse period. Figure 5(c) shows our data can be fit to a double exponential recovery with $\tau_1 = 0.92 \mu\text{s}$ and $\tau_2 = 11.7 \mu\text{s}$. These are exceptionally long lifetimes for typical electronic and phononic degrees of freedom; this suggests a metastable phase coexistence developing at this temperature. Such phase coexistence is associated with a first-order phase transition, which leads us to conclude that the CDW phase transition in CsV_3Sb_5 is discontinuous.

To clarify the optical characterization data, Lily Hallett performed first-principles density functional theory (DFT) calculations of the phonon mode frequencies. The room temperature space group of these materials is $P6/mmm$, shown in Figure 6(a). Figure 6(c) shows the full phonon dispersion relation. The calculations predict two unstable modes: one at the M point ($k_z = 0$) and one at the L point ($k_z = \pi/c$), shown in Figure 6(b). A symmetry analysis indicates that the irreducible representations of the modes are M_1^+ and L_2^- . The M point is of particular interest in this material, as it connects saddle points in the electronic band structure and is associated with a Peierls-like nesting-driven instability [15].

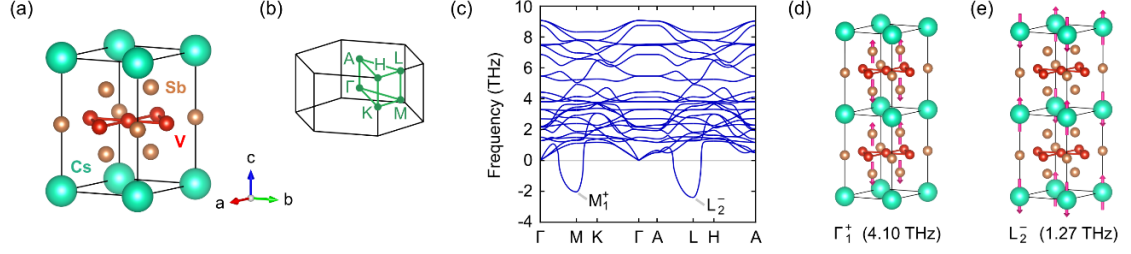


Figure 6: First-principles phonon calculations. (a) Unit cell for CsV_3Sb_5 . The vanadium atoms (red) form a kagome net and are coordinated with in-plane and out-of-plane antimony atoms. (b) First Brillouin zone of the hexagonal lattice, with high-symmetry points labeled. (c) Calculated phonon dispersion relations reveal two unstable modes with imaginary frequencies: one at the M point with irreducible representation M_1^+ , and the other at the L point with irreducible representation L_2^- . (d) Illustration of the fully symmetric Γ_1^+ phonon at 4.10 THz detected at all temperatures. (e) Illustration of the L_2^- phonon at 1.27 THz detected below T_{CDW} .

It is widely believed that a simultaneous condensation of three M-point modes drives the CDW phase transition [17]. This type of 3Q order, which we label MMM, leads to a fully symmetric breathing mode with two possible configurations: a "Star of David" distortion, or a tri-hexagonal "inverse Star of David" distortion [17]. However, other possible combinations of M- and L-point modes exist: MML, MLL, and LLL. To determine which of these four possibilities is the most likely ground state in CsV_3Sb_5 , we calculated their energies as a function of atomic displacement. We found that the lowest energy state in fact corresponds to the tri-hexagonal MLL distortion, rather than the expected MMM distortion. This ground state distortion can be described as in-plane tri-hexagonal distortions with a c-axis shift of one lattice vector between neighboring kagome planes. This conclusion is supported by our experimental determination that the CDW phase transition is first-order, which eliminates the odd-parity MML and LLL distortions.

The DFT calculations reveal symmetry information about the phonon modes we discovered. The γ mode at 4.1 THz, which is detected at all temperatures, must be a fully

symmetric mode, as it is not affected by the CDW phase transition. The DFT calculations find a single Γ_1^+ (A_{1g}) mode which exactly matches the experimental frequency. This mode involves coherent motion of the out-of-plane antimony atoms along the c axis towards/away from the kagome planes, shown in Figure 6(d). The excellent agreement we find between our experiment and the theory reinforces the accuracy of our DFT calculations.

Next, we consider the α mode detected at 1.3 THz. This mode appears abruptly at T_{CDW} and consequently represents a phonon that becomes Raman active in the CDW phase. This implies that the α mode must have either M_1^+ or L_2^- symmetry. Our DFT calculations suggest the presence of an L_2^- phonon with a frequency of 1.27 THz which involves cesium atom motion along the c axis, shown in Figure 6(e). The observation of this mode serves as strong experimental confirmation that the CDW order in CsV_3Sb_5 is modulated along the c axis, which is consistent with an MLL distortion. These are not the only phonons predicted to become Raman active in the CDW phase: our DFT data predicts an M_1^+ phonon at 3.63 THz and a second L_2^- phonon at 3.67 THz. Weak spectral intensity is present in the Fourier map below T_{CDW} within this frequency range. Our experiment could detect these modes, however their amplitude is much weaker than the α mode.

Finally, we examine the β mode, which is spread over a broad spectral range centered at 3.1 THz. This feature is rather unusual because it appears well below T_{CDW} at $T^* \approx 60 K$. We believe this resonance is related to the uniaxial order observed below T_{CDW} by scanning tunneling microscopy experiments [13], [14], [18]. Such a uniaxial ordering would break the C_6 rotational symmetry of the crystal and result in a myriad of newly Raman-active modes excitable by a pump pulse, several with frequencies near 3.1 THz. In fact, MLL order already breaks the C_6 rotational symmetry (whereas MMM order does not), which may offer

a natural explanation for the uniaxial order reported in the AV_3Sb_5 material system. We further speculate that the lower onset temperature of the uniaxial order may be related to an order-disorder crossover associated with c-axis coherence, as there are three equivalent MLL configurations which are distinguished only by the direction of the lateral plane-to-plane shift of the tri-hexagonal CDW pattern.

D. Conclusion

In summary, we used a combination of coherent phonon spectroscopy experiments and DFT calculations to investigate the CDW state in CsV_3Sb_5 . Our data showed that the CDW phase transition is first order and corresponds to a condensation of three optical phonon modes at one M and two L points. This ordering, distinct from the more commonly accepted “MMM” ordering, involves interlayer modulation of the CDW along the c axis and may offer a natural explanation for the uniaxial order observed at lower temperatures.

III. Conclusion

Optical techniques such as SHG and pump-probe spectroscopy were instrumental in our pursuit to investigate the intriguing properties of quantum materials. The direct measurement of the ferroelectric order parameter in $SrTiO_3$ was only possible by utilizing SHG measurements, and pump-probe spectroscopy was necessary to characterize the CDW state of CsV_3Sb_5 . Quantum materials provide a promising platform for future technologies. Progress made in this field could eventually lead to world-changing breakthroughs such as room temperature superconductivity and fault-tolerant quantum computing.

References

- [1] L. Zhao, D. Torchinsky, J. Harter, A. de la Torre, and D. Hsieh, “Second Harmonic Generation Spectroscopy of Hidden Phases,” in *Encyclopedia of Modern Optics*, Elsevier, 2018, pp. 207–226. doi: 10.1016/B978-0-12-803581-8.09533-3.
- [2] R. E. Newnham, *Properties of materials: anisotropy, symmetry, structure*. Oxford ; New York: Oxford University Press, 2005.
- [3] N. Ratcliff, L. Hallett, B. R. Ortiz, S. D. Wilson, and J. W. Harter, “Coherent phonon spectroscopy and interlayer modulation of charge density wave order in the kagome metal CsV_3Sb_5 ,” *Phys. Rev. Mater.*, vol. 5, no. 11, p. L111801, Nov. 2021, doi: 10.1103/PhysRevMaterials.5.L111801.
- [4] A. Verma, S. Raghavan, S. Stemmer, and D. Jena, “Ferroelectric transition in compressively strained SrTiO_3 thin films,” *Appl. Phys. Lett.*, vol. 107, no. 19, p. 192908, Nov. 2015, doi: 10.1063/1.4935592.
- [5] K. Ahadi, L. Galletti, Y. Li, S. Salmani-Rezaie, W. Wu, and S. Stemmer, “Enhancing superconductivity in SrTiO_3 films with strain,” *Sci. Adv.*, vol. 5, no. 4, p. eaaw0120, Apr. 2019, doi: 10.1126/sciadv.aaw0120.
- [6] R. W. Boyd, *Nonlinear optics*, 3rd ed. Amsterdam ; Boston: Academic Press, 2008.
- [7] J. W. Harter, Z. Y. Zhao, J.-Q. Yan, D. G. Mandrus, and D. Hsieh, “A parity-breaking electronic nematic phase transition in the spin-orbit coupled metal $\text{Cd}_2\text{Re}_2\text{O}_7$,” *Science*, vol. 356, no. 6335, pp. 295–299, Apr. 2017, doi: 10.1126/science.aad1188.
- [8] F. H. Yu *et al.*, “Concurrence of anomalous Hall effect and charge density wave in a superconducting topological kagome metal,” p. 11.
- [9] Y.-X. Jiang *et al.*, “Discovery of unconventional charge order in kagome superconductor KV_3Sb_5 ,” *ArXiv201215709 Cond-Mat*, Apr. 2021, Accessed: Apr. 23, 2021. [Online]. Available: <http://arxiv.org/abs/2012.15709>
- [10] B. R. Ortiz *et al.*, “New kagome prototype materials: discovery of KV_3Sb_5 , RbV_3Sb_5 , and CsV_3Sb_5 ,” *Phys. Rev. Mater.*, vol. 3, no. 9, p. 094407, Sep. 2019, doi: 10.1103/PhysRevMaterials.3.094407.
- [11] C. C. Zhao *et al.*, “Nodal superconductivity and superconducting domes in the topological Kagome metal CsV_3Sb_5 ,” *ArXiv210208356 Cond-Mat*, Mar. 2021, Accessed: Mar. 18, 2021. [Online]. Available: <http://arxiv.org/abs/2102.08356>
- [12] Z. Zhang *et al.*, “Pressure-induced Reemergence of Superconductivity in Topological Kagome Metal CsV_3Sb_5 ,” p. 10.
- [13] K. Y. Chen *et al.*, “Double superconducting dome and triple enhancement of T_c in the kagome superconductor CsV_3Sb_5 under high pressure,” p. 15.
- [14] Z. Liang, X. Hou, W. Ma, F. Zhang, P. Wu, and Z. Zhang, “Three-dimensional charge density wave and robust zero-bias conductance peak inside the superconducting vortex core of a kagome superconductor CsV_3Sb_5 ,” p. 12.
- [15] B. R. Ortiz *et al.*, “ CsV_3Sb_5 : A Z_2 Topological Kagome Metal with a Superconducting Ground State,” *Phys. Rev. Lett.*, vol. 125, no. 24, p. 247002, Dec. 2020, doi: 10.1103/PhysRevLett.125.247002.
- [16] E. Uykur, B. R. Ortiz, S. D. Wilson, M. Dressel, and A. A. Tsirlin, “Optical detection of charge-density-wave instability in the non-magnetic kagome metal KV_3Sb_5 ,” *ArXiv210307912 Cond-Mat*, Mar. 2021, Accessed: Mar. 18, 2021. [Online]. Available: <http://arxiv.org/abs/2103.07912>

- [17] H. Tan, Y. Liu, Z. Wang, and B. Yan, “Charge density waves and electronic properties of superconducting kagome metals,” *ArXiv210306325 Cond-Mat*, Mar. 2021, Accessed: Mar. 18, 2021. [Online]. Available: <http://arxiv.org/abs/2103.06325>
- [18] H. Zhao *et al.*, “Cascade of correlated electron states in a kagome superconductor CsV₃Sb₅,” p. 12.